pubs.acs.org/Biomac

Article

Enhanced Hydrogen Bonding by Urea Functionalization Tunes the Stability and Biological Properties of Peptide Amphiphiles

Published as part of Biomacromolecules virtual special issue "Peptide Materials".

Huihua Xing, Caleb Wigham, Sieun Ruth Lee, Aramis J. Pereira, Luana J. de Campos, Agustín S. Picco, Cristián Huck-Iriart, Carlos Escudero, Laura Perez-Chirinos, Sandun Gajaweera, Jeffrey Comer, Ivan R. Sasselli, Samuel I. Stupp, R. Helen Zha, and Martin Conda-Sheridan*

Cite This: *Biomacromolecules* 2024, 25, 2823−2837

Read Online

ACCESS | Metrics & More | Article Recommendations | Supporting Information

ABSTRACT: Self-assembled nanostructures such as those formed by peptide amphiphiles (PAs) are of great interest in biological and pharmacological applications. Herein, a simple and widely applicable chemical modification, a urea motif, was included in the PA's molecular structure to stabilize the nanostructures by virtue of intermolecular hydrogen bonds. Since the amino acid residue nearest to the lipid tail is the most relevant for stability, we decided to include the urea modification at that position. We prepared four groups of molecules (13 PAs in all), with varying levels of intermolecular cohesion, using amino acids with distinct β-sheet promoting potential and/or containing hydrophobic tails of distinct lengths. Each subset contained one urea-modified PA and nonmodified PAs, all with the same peptide sequence. The varied responses of these PAs to variations in pH, temperature, counterions, and biologically related proteins were examined using microscopic, X-ray, spectrometric techniques, and molecular simulations. We found that the urea group contributes to the stabilization of the morphology and internal arrangement of the assemblies against environmental stimuli for all peptide sequences. In addition, microbiological and biological studies were performed with the cationic PAs. These assays reveal that the addition of urea linkages affects the PA−cell membrane interaction, showing the potential to increase the selectivity toward bacteria. Our data indicate that the urea motif can be used to tune the stability of a wide range of PA nanostructures, allowing flexibility on the biomaterial's design and opening a myriad of options for clinical therapies.

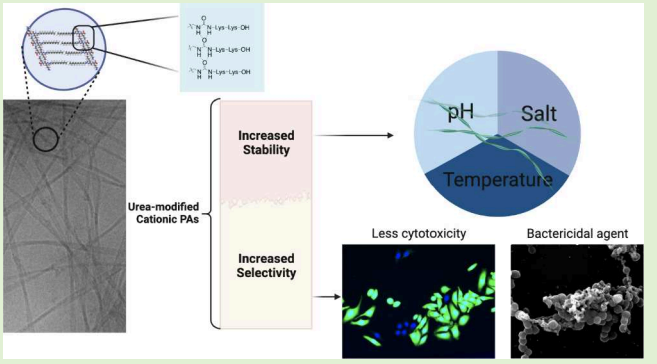

1. INTRODUCTION

Functional supramolecular structures, including DNA and proteins, are essential for life. Self-assembling molecules, such as the peptide amphiphiles (PAs), can form supramolecular architectures by virtue of noncovalent interactions.[1] These bioinspired materials can mimic the function of biomacromolecules while also achieving unprecedented new properties. A basic PA molecule contains one or more lipid tails linked to a peptide sequence. Then, linker region and bioactive epitopes (such as short peptide sequences or DNA segments of small molecules) can be included as part of the molecular structure. The groups present on the PA allow them to be responsive to environmental cues, including pH, temperature, electrolytes, and biomolecules.[2] As a result, supramolecular behavior can be tuned "on demand" by modifying noncovalent interactions through engineering the peptide sequence, changing the lipid portion of the PA, or the linkage between the peptide and lipid segments. However, the lack of covalent bonds within the nanostructure may pose a challenge when the desired application requires high stability and robustness. Several factors can contribute to the responsiveness and biological activity of a PA nanostructure, including supramolecular shape[3,4] and size,[5,6] amino acid sequence, and internal cohesion.[7] Thus, achieving control at the supramolecular level is essential to regulate the biological response of PA nanostructures.

For example, previous studies have shown that acylation of the N-terminus can affect thermal stability[8] and increase amphiphilicity and cell cytotoxicity.[1,7] Further, factors such as intermolecular interactions[3] and filament shape[7,9] influence interactions between PA assemblies and phospholipid

Received: December 31, 2023
Revised: March 29, 2024
Accepted: March 29, 2024
Published: April 11, 2024

https://doi.org/10.1021/acs.biomac.3c01463
Biomacromolecules 2024, 25, 2823−2837

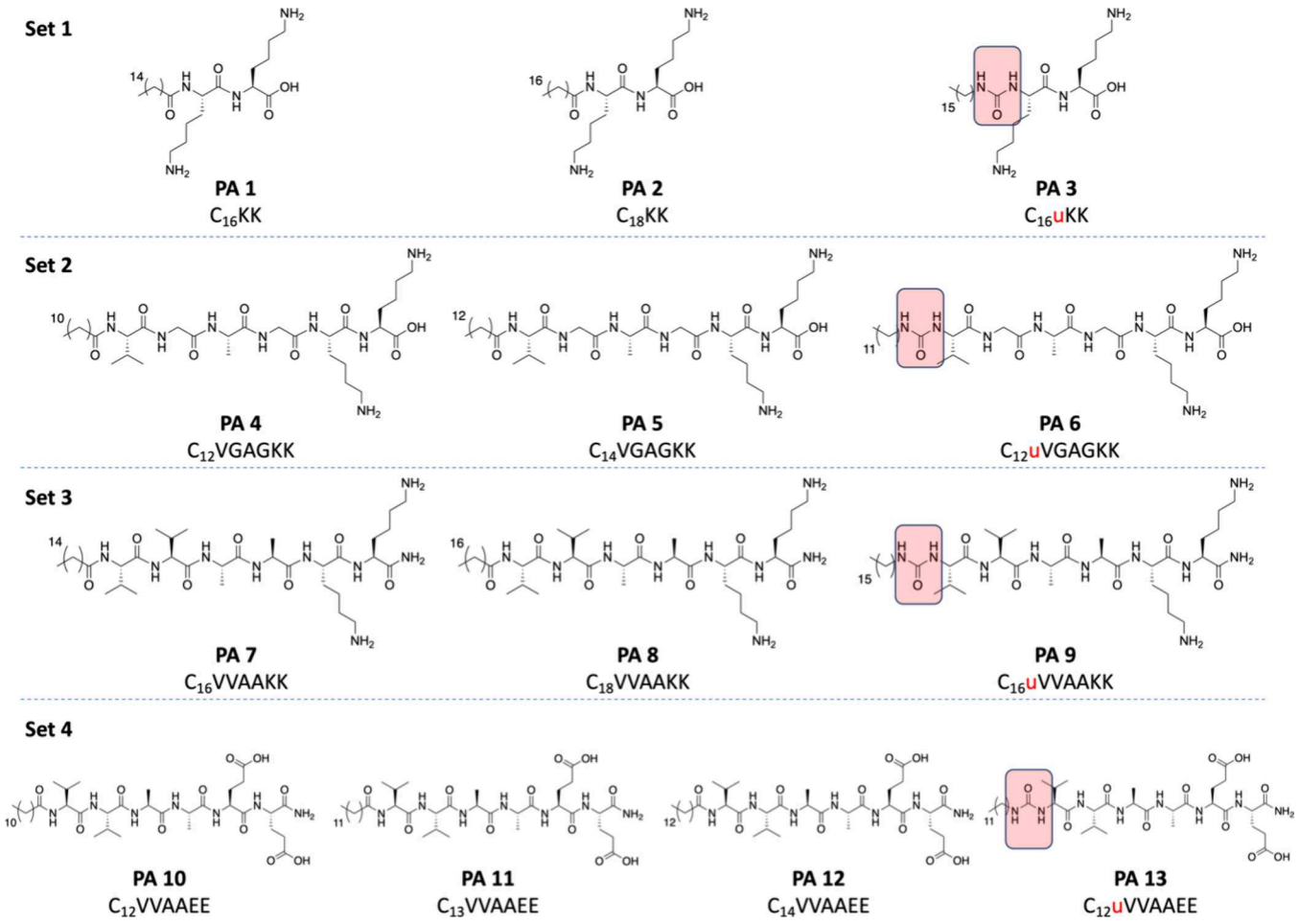

Figure 1. Chemical structure of PAs. Set 1 contains **PA 1−3**: [C16]K_2, [C18]K_2, and [C16]uK_2 (top panel, from left to right). Set 2 contains **PA 4−6**: [C12]VGAGK_2, [C14]VGAGK_2, and [C12]uVGAGK_2, Set 3 contains **PA 7−9**: [C16]$V_2A_2K_2$, [C18]$V_2A_2K_2$, and [C18]u$V_2A_2K_2$, and Set 4 contains anionic **PA 10−13**: [C12]$V_2A_2E_2$, [C13]$V_2A_2E_2$, [C14]$V_2A_2E_2$, and [C12]u$V_2A_2E_2$. [C**n**] = carboxylic acid tail with "**n**" number of carbons.

membranes and, as a consequence, cell viability. In the case of cationic surfactants, the ability to interact and penetrate cell membranes is related to the high affinity of their cationic head groups for the polyanions that constitute a protective barrier.[10,11] Therefore, we can assume that modulating the cationic charge and the dynamics of the assembly will greatly affect the interaction. Thus, the pH responsiveness of PA nanostructures may be tuned by changing the ionization state (related to the pK_a of head groups), which alters electrostatic interactions and overall balance among noncovalent interactions.[12,13]

Therefore, the nature of a functional group may affect the intramolecular interactions of self-assembling systems with a profound effect on the supramolecular level. We have been interested in studying the effect of different hydrogen bond donors on the properties of PA nanostructures. The urea group possesses an additional hydrogen bond donor when compared with an amide and a slightly higher pK_a. Beuerman's group also studied the effect of internal cohesion by performing simulations that suggest hydrogen bonding plays a key role in the interaction between antimicrobial peptides and negatively charged membranes.[14] Further, Bukovsky's laboratory also reported that the presence of urea groups increased the tendency to assemble and the bioactivity of a series of urea-based gemini antimicrobial surfactants.[15] These examples show that specific molecular modifications can modify biological activity. We have observed, as reported in our previous study, that the inclusion of a urea motif between hydrophobic and hydrophilic segments (which confers additional hydrogen bonding capacity as predicted theoretically in our previous paper[16]) improved PA hydrogel stability and enhanced its ability to support cell adhesion and spreading relative to similar molecules that lacked the urea group.[16]

Herein, we report the influence of urea addition on the PA's morphological response to environmental changes. To test our hypothesis that the extra hydrogen bonds provided by the urea (as compared to those provided by an amide) can enhance the structural stability against stimuli, we designed four sets of PAs. Three sets are cationic, containing two C-terminated Lys while one is anionic, containing two C-terminal Glu (Figure 1). Each individual set contains PAs with a shorter alkyl tail (**PA 1**, **4**, **7**, and **10**), a longer alkyl tail (**PA 2**, **5**, **8**, and **11−12**), and their urea-modified PA analog (**PA 3**, **6**, **9**, and **13**). The three different peptide sequences (KK, VGAGKK, and VVAAKK) were designed to promote a range of intermolecular cohesion. Meanwhile, different alkyl tail lengths were included to explore the interplay between the urea modification and hydrophobic segments that provide different lipophilicity (which will affect hydrophobic collapse). This allowed us to assess the influence of urea modification on distinct PA systems. Initially, we

https://doi.org/10.1021/acs.biomac.3c01463
Biomacromolecules 2024, 25, 2823−2837

studied the morphology and internal arrangement of the PA assemblies as a function of solution pH and temperature in dried samples via transmission electron microscopy (TEM), atomic force microscopy (AFM), and Fourier transform infrared (FT-IR) spectroscopy, and in solution via small-angle X-ray scattering (SAXS), thioflavin T (ThT), differential scanning calorimetry (DSC), and circular dichroism (CD). The disruption of the nanostructure's morphology by ionic inorganic salts was studied by TEM and molecular dynamics (MD) simulations. Then, we evaluated the effect of the urea on normal and cancer cell lines. We also assessed the antimicrobial effect including the alterations the nanostructures produce on the membrane potential and permeability. The results indicate the role of the urea group on the nanostructures' stability against pH, salt concentration, denaturizing agents, and heat. We also indicate how the urea modulates the biological activity of PA nanostructures toward bacteria and human cells.

2. EXPERIMENTAL SECTION

2.1. Synthesis and Characterizations. All PAs were synthesized using standard Fmoc solid-phase peptide synthesis on a 0.3-mmol scale on Resin as reported.[16] Urea-linked peptides were synthesized by coupling the peptide segment to a dodecyl isocyanate molecule (8 equiv) with 1:1 dimethylsulfoxide (DMSO)/dimethylformamide (DMF) (vol %, enough solvent to dissolve the molecules). The obtained molecules were purified and characterized as reported but with a solvent mixture of acetonitrile and water; both containing 0.1% trifluoroacetic acid (TFA) by volume. The mass was confirmed by matrix assisted laser desorption/ionization (MALDI) (Bruker Autoflex maX). The organic solvent was removed, and the samples were frozen and lyophilized (FreeZone, Labconco) after adjusting pH to 7.0 (0.1 M HCl and NaOH).

2.2. Preparation of PA Assemblies. Lyophilized PAs were dissolved in high performance liquid chromatography (HPLC)-grade water/buffer to a certain concentration. The samples were annealed at 80 °C for 2 h (Isotemp hot plate, Fisher Scientific, or spectrometer heating unit), slowly cooled to room temperature, and aged before testing. The final pH was confirmed by a pH meter.

2.3. AFM. PA samples (1 mg/mL) were deposited on aminopropyl silatrane mica and scanned according to the protocol in our previous study.[16]

2.4. Transmission Electron Microscopy. The PAs were prepared to give a final concentration of 1 mg/mL and aged for the required amount of time before the experiments. The operation followed the protocol described in our previous work.[16]

2.5. Small-Angle X-ray Scattering (SAXS). SAXS data were collected at BioSAXS/HP-Bio beamline ID7A (CHESS, Cornell High-Energy Synchrotron Source, Ithaca, USA) and the BL11 NCD-SWEET beamline (ALBA Synchrotron Light Source, Cerdanyola del Vallès, Barcelona, Spain). For experiments at CHESS, the X-ray beam was collimated to 250 × 250 μm, and the sample-to-detector distance was 1722 mm, with an energy of 13.437 keV and wavelength of 0.922679 Å. PA solutions prepared at 5 mg/mL were aged overnight before the scanning. The data were collected by a Dectris Eiger 1 M detector. For measurements at the ALBA, experiments were done using 1.5 mm external diameter glass capillaries. The incoming beam energy was set at 12.4 keV with a 6700-mm sample to detector distance. 2D patterns were recorded in a Pilatus 1 M (Dectris, Switzerland) detector. Isotropic 2D patterns were integrated using pyFAI library.[17] Temperature control was done using a Linkam holder. In addition, preliminary experiments were performed at the SAXS-1 beamline of the Brazilian Synchrotron Light Laboratory (LNLS-CNPEM, Campinas, Brazil).

2.6. ThT Assay. The PAs were prepared at 10 mM in different pH buffers, annealed, and aged overnight before the assay. ThT stock solution was prepared at 2 mM and diluted to a final concentration of 100 μM. Then, it was incubated with PA solutions (final concentration of 1 mM) in the dark for about 2 h to achieve efficient binding. The fluorescence spectrum was collected with excitation at 440 nm and emission between 450 and 550 nm, with an interval of 10 nm.

2.7. Nano Differential Scanning Calorimetry (NanoDSC). NanoDSC measurements were carried out on a TA Instruments NanoDSC, Model 602000. Lyophilized samples of PAs **10**–**13** were dissolved in 1:1 phosphate buffered saline (PBS)/H_2O at 4 °C, diluted to 1 mg/mL, and degassed for 20 min at 25 °C under 25 in Hg vacuum. Conditioning scans using buffer were performed prior to data collection. Background and PA sample scans were performed in the range of 15–130 °C at a scanning rate of 1 °C/min. Samples were pressurized to 3 atm and allowed to equilibrate for 10 min prior to data collection.

2.8. FT-IR Spectroscopy. PA solutions were lyophilized in the target conditions to be dissolved at 10 mM in D_2O, undergoing the same heat–cooling procedure as described in the preparation of PA assemblies. The measurements were performed on an Invenio-X Bruker FT-IR. The sample was placed between two 32 mm CaF2 windows separated by a Teflon spacer of 50 μm. Final spectra are the result of 25 scans with 1 cm^{-1} resolution, and the data were corrected by subtracting the absorptions from the air and the D_2O.

2.9. Fluorescent Resonance Energy Transfer (FRET). The DiO and DiI were prepared at 1 mg/mL in DMSO as stock solutions, separately. These two dye solutions were added to PA aqueous solutions (annealed and aged samples) to make a final concentration of PA at 250 and dye at 50 μg/mL. The resulting DiO-PA solution and DiI-PA solution were settled down overnight and filtered with 0.45 μm filter to remove the insoluble residues. Then, 50 μL of a DiO-PA solution was mixed with 50 μL of a DiI-PA solution. The fluorescence spectra of emission wavelength from 490 to 640 nm at an excited wavelength of 484 nm were recorded by a SpectraMax microplate reader at time spot 0 min, 1, 2, 3, and 4 h.

2.10. Molecular Model. The molecular models were built using the VMD software package[18] (version 1.9.4) and Packmol[19] (version 18.002). For each of the three PAs considered (**PA 1**, **PA 2**, and **PA 3**), we created two models with different initial conditions. The protonation states were taken to be those expected near neutral pH: lysine side chains were protonated (NH_3^+), and the PA C-termini were in their deprotonated carboxylate (CO_2^-) form, giving each a net charge of −1. All of the models contained 256 PA molecules of a single type. For the first set of models, Packmol[19] was used to randomly pack PAs into a cube of side length 80 Å, while, for the second set of models, they were packed into a 40 Å cube. The systems constituted 256 PA molecules placed in a cubic box with a side length of 105 Å using Packmol. Using these two distinct initial conditions allowed us to design a simulation protocol in which the results did not depend on the initial PA configuration. Each of the six systems was solvated in a (115 Å)[20] box of CHARMM standard TIP3P water. Salt was added to neutralize the systems and represent a 280 mmol/L NaCl concentration using the SLTCAP (screening layer tally by container average potential) method developed by Schmidt et al.[20] This resulted in systems comprising 121,000–135,000 total atoms, including 32,000–36,000 water molecules, 80–100 Na^+ ions, and 340–356 Cl^- ions. After equilibration at 295 K and 1.01325 bar (using thermostat and barostat algorithms as detailed below), the system sizes were in the range (105–109 Å).[20] MD protocols, simulated annealing, and characterization of the PA aggregates are described in the SI.

2.11. Cell Culture. All cell lines were cultured using ATCC protocols for all of the experiments. The cell was cultured at 37 °C and 5% CO_2. The cytotoxicity was accessed by cell proliferation kit II (XTT) tests, with seeding cell density of 4×10^4 (HEp2, HaCaT, and HEK 293T), 2×10^4 (MCF-10A), and 6×10^4 (HCC70).

2.12. Live and Dead Assay. HEp2 suspension of density 1×10^4 was seeded on the plate and was incubated for 24 h. The media was replaced with the PA-diluted solutions. The treated plates were incubated for the desired time at 37 °C. Calcein AM and Hoechst 33342 were diluted with PBS to make a final 1 μM mixture solution.

https://doi.org/10.1021/acs.biomac.3c01463
Biomacromolecules 2024, 25, 2823–2837

The cells were stained by the mixture for 15 min at 37 °C. The dye was removed, and PBS was added before imaging (EVOS Fluorescent Imaging Microscope). Statistical analysis was performed using Prism 9.

2.13. Microbiological Assays. All bacterial cultures were made by the direct colony suspension method adjusted to 0.5 McFarland and diluted with Muller−Hinton broth to a concentration of 1×10^6 CFU/mL. A stock PA water solution of 2 mg/mL was prepared, annealed, and aged overnight. The serial dilution of PA was prepared at specific concentration ranges (100 μL/well). 10 μL of bacteria-diluted suspension was added to the PA plate to get a final concentration of 1×10^5 CFU/mL. The plates were incubated for 18−22 h at 37 °C. A 0.1% triphenyl tetrazolium chloride solution was added to the treated bacteria plates. The minimum inhibitory concentration (MIC) was defined as the lowest drug concentration that showed no visible bacterial growth. The minimum bactericidal concentration (MBC) was determined by seeding suspensions on Muller−Hinton agar plate. The plates were incubated for 18−22 h at 37 °C, and the MBC was determined as the lowest drug concentration that showed no visible bacterial growth. All experiments were performed in triplicate.

2.14. Cytoplasmic Membrane Depolarization Assay. *A. baumannii* cells were washed three times (centrifugation at 3500 rpm for 5 min) and resuspended in 5 mM HEPES and 20 mM glucose (pH 7.4) at 0.3 McFarland turbidity standard. A final concentration of 1 μM DiSC3(5) was used to stain the cells for 30 min at 37 °C. 160 μL of bacteria was transferred to a 96-well plate. The fluorescence intensity was measured at an excitation wavelength 622 nm and emission wavelength 670 nm. After that, PA solutions and polymyxin B were added to the wells followed by measuring the fluorescence intensity for 60 min, with 2 min intervals.

2.15. Membrane Permeability Assay. *A. baumannii* cells were washed and resuspended in 5 mM HEPES and 20 mM glucose (pH 7.4) at a 0.3 McFarland turbidity standard. A final concentration of 7.5 μg/mL propidium iodide (PI) was added, and the system was incubated for 30 min at 37 °C. After the treatment, the fluorescence intensity was monitored for 60 min with 2 min intervals at an excitation wavelength of 535 nm and an emission wavelength of 615 nm.

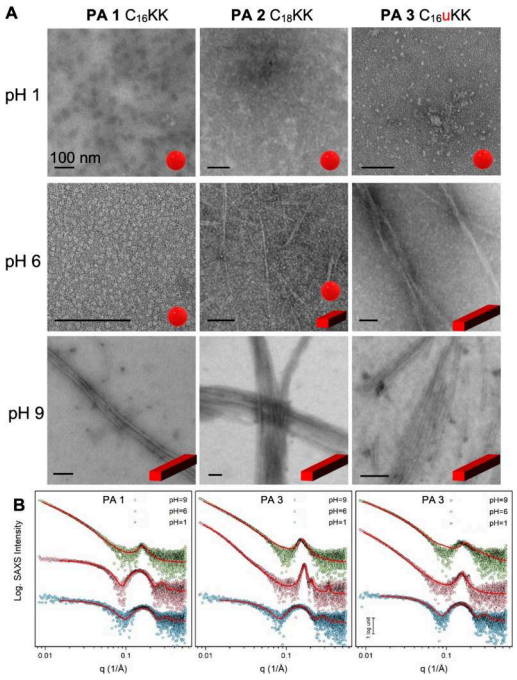

Figure 2. Morphological transitions of **PA 1−3** nanostructures response to pH changes. (A) TEM images of **PA 1−3** in pH 1, 6, and 9 buffer at 1 mg/mL, from left to right, respectively. (B) SAXS curves of **PA 1−3** from pH 1 to pH 9. The PAs were prepared at 5 mg/mL to increase signal-to-noise ratio. A transition between micelles and structured assemblies can be observed for the three PAs with increasing pH. This transition happened above pH 6 for **PA 1**, while for **PA 2−3**, it happened above pH 9. The red lines superimposed over the experimental data are the best fit using a spherical core−shell model for **PA 1−3** at pH 1 and **PA 1** at pH 6, and the Guinier-Porod model combined with Lorentzian functions for **PA 2−3** at pH 6, and **PA 1−3** at pH 9 as explained in the main text.

3. RESULTS AND DISCUSSION

3.1. Urea Modification Stabilizes Nanostructures' Shape against pH Changes. *3.1.1. Morphological Transition Induced by pH Changes.* The charged groups, which are exposed to the solvent, change the ionization state depending on the media pH. This, in turn, can alter the supramolecular morphology. To evaluate the effect of the urea modification, we performed TEM to visualize the PA nanostructure's morphology at different pH. As shown in the left panel of Figure 2A, **PA 1** ($\mathbf{C_{16}K_2}$) assembled into spherical objects from pH 1 (Figure 2A, top) to pH 6 (Figure 2A, middle). Fibril structures can be achieved at pH 7.4 (Figure S5) and 9 (Figure 2A, bottom). A similar micelle-fibril morphological transition occurs with **PA 2** ($\mathbf{C_{18}K_2}$, middle panel of Figure 2A) and **PA 3** ($\mathbf{C_{16}uK_2}$, right panel of Figure 2A). This result was expected because at pH 1, the fully protonated amine produces a strong intermolecular repulsion, preventing the formation of elongated objects. At pH 6, the repulsion is reduced because not all side chains are protonated (the pK_a is affected by the local environment in supramolecular systems[19]). The longer alkyl tail of **PA 2** provides stronger hydrophobic collapse compared to **PA 1**, promoting molecular association and allowing the formation of short fibrils. However, the hydrophobic collapse of **PA 2** is not enough to offset the molecular repulsion and promote long filament formation below pH 7.4. Interestingly, urea-modified **PA 3** assembles into elongated objects at pH 6. This confirms our hypothesis that the extra hydrogen bonds provided by urea modification counterbalance the intermolecular repulsion at acidic pH. This result suggests the increased cohesion provided by the urea group is stronger than the hydrophobic collapse raised by two more methylenes, since **PA 3** forms elongated objects at a pH lower than **PA 2**.

AFM (Figure S6) also shows a similar tendency of morphological transition behavior, indicating that the stability against pH change is **PA 3** > **PA 2** > **PA 1**. Cryo-EM was used to visualize the nanostructures in solution at pH 6. As shown in Figure S7, **PA 3** formed elongated objects while **PA 1** and **PA 2** did not, further confirming the fibril-promoting effect of the urea modification. Finally, the PA assemblies at various pH values were studied by SAXS (Figure 2B; modeling details can be found in Figures S8−S10, and Tables S1 and S2). At pH 1 for the three **PAs** (and pH 6 for **PA 1**), the PAs exhibit curves corresponding to spheroidal objects (red curves in Figure 2B) that can be modeled as core−shell micelles with diameters around 6 nm. At higher pH (pH 9 for the three **PAs** and pH 6 for **PA 2 and PA 3**), SAXS patterns showed a linear slope of −2, an indication of a 2D structure. The change in pH alters the electrostatic interaction between PAs which was reflected not only in the morphology but also in the aggregation factor observed as the intermediate zone. The broad and intense peak around 1.6 nm^{-1} (interplanar distance, $D_{int} = 2\pi/q$, ca. 4 nm) can be attributed to the stacking of lamellar planes At pH = 6, **PA 2** (slightly) exhibited the second reflection of the lamellar

https://doi.org/10.1021/acs.biomac.3c01463
Biomacromolecules 2024, 25, 2823−2837

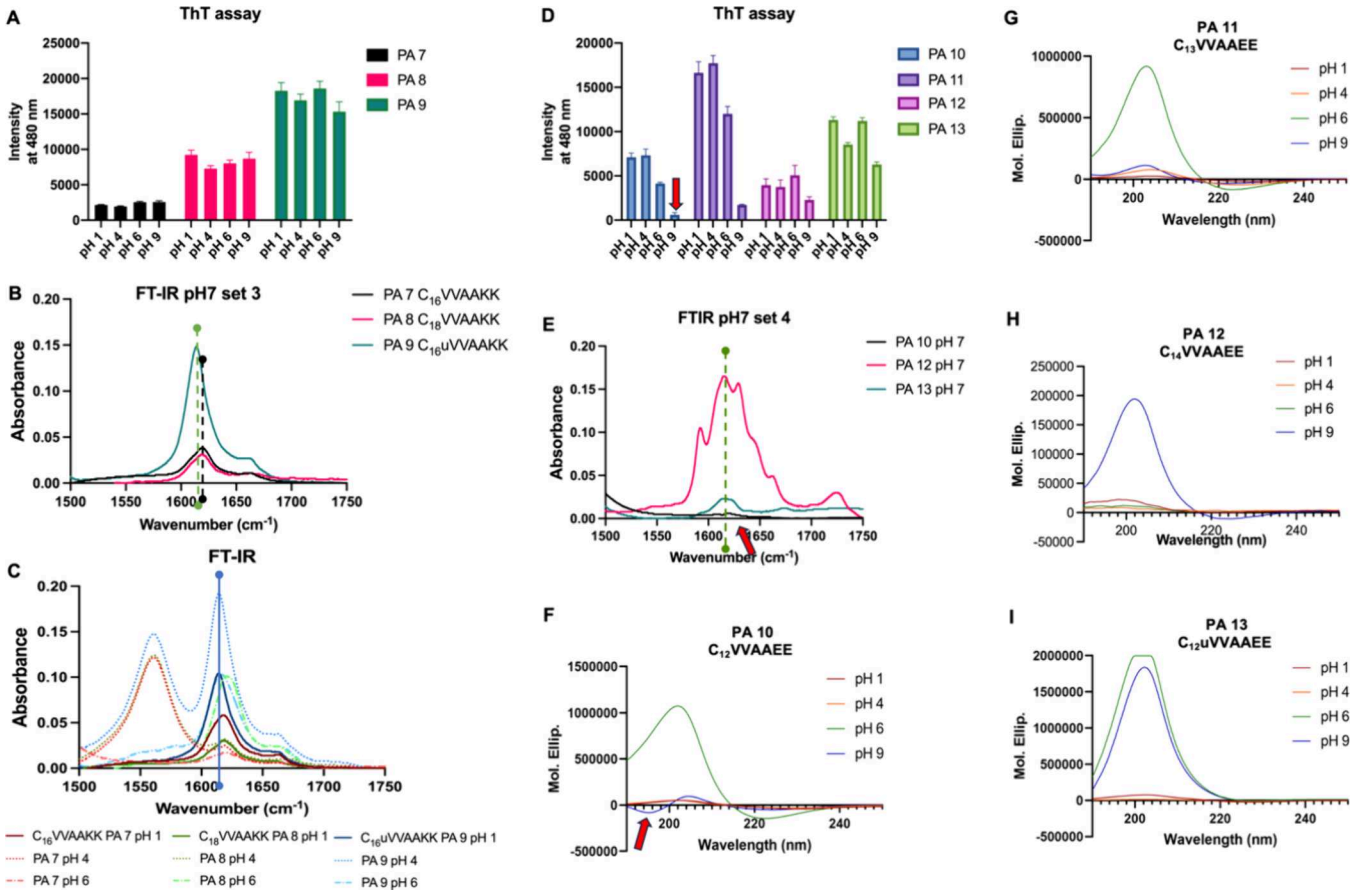

Figure 3. Internal arrangement study of Set 3 (**PA 7−9**) and Set 4 PAs (**PA 10−13**) from pH 1 to pH 9. (A) ThT assay of **PA 7−9** at pH 1, 4, 6, and 9, respectively. (B) FT-IR spectra of **PA 7−9** at pH 7. (C) FT-IR spectra of **PA 7−9** at pH 1, 4, and 6. (D) ThT assay of **PA 10−13** at pH 1, 4, 6, and 9, respectively. (E) FT-IR spectra of **PA 10, 12,** and **13** at pH 7. (F−I) CD spectra of **PA 10−13** at pH 1, 4, 6, and 9. All assays were performed with annealed and aged samples in pH buffer solutions. Data in A and D are mean ± s.d. with n = 3 replicates.

structure at twice the q value. In addition, it presented a new peak at ∼ 2.0 nm^{-1} (D_{int} ∼3.1 nm), which might derive from the correlation between PA molecules within the lamellar planes. Due to highly stacking polydispersity, curves were modeled using a semiempirical Guinier−Porod function[21] combined with Lorentzian functions for the diffraction contribution. The differences in morphology at the transition pH (approximately 6) seen by the different techniques might be caused by distinct sample preparation procedures and operator bias in image acquisition. PI.[22,23] Overall, the SAXS data indicate that the urea-modified **PA 3** has a similar or stronger ability than **PA 2** to form fibrous structures under acidic conditions (despite strong electrostatic repulsion).

The PAs in Set 2 have a longer peptide sequence when compared to Set 1, VGAG, designed to provide more intermolecular hydrogen bonds. Our theory is this will result in more cohesive nanostructures than those in Set 1. The pH-responsive morphological transitions are shown in Figure S11A. At pH 1, urea-modified **PA 6** formed cylindrical micelles/short fibers, while **PA 4** and **PA 5** formed large aggregates. The order of the morphological transition pH for Set 2 PA is **PA 6** > **PA 5** > **PA 4**. This result validates the observation above that the additional hydrogen bond contributed by the urea counteracts the repulsion at low pH. The SAXS for this set of PAs (curves can be found in Figure S10) shows that only **PA 6** displays a pattern consistent with a spherical micelle at pH 1. At pH 6 and 9, the particles were mainly ribbon-like structures, similar at all pH conditions for **PA 4** and **5**. Interestingly, SAXS intensities were solely determined by the form factor (how the object scatters X-rays based on its size, shape, and electronic density distribution), and no structure factor was observed (i.e., no periodic order between the objects was evidenced). A model of a single ribbon was used for the form factor, as detailed in our previous work,[12] and can be found in Table S2. Set 3 PAs (**PA 7−9**) are designed with a stronger β-sheet forming region: VVAA.[12] All PAs in this set formed elongated objects from pH 1 to 9, as observed from TEM (Figure S11B) and AFM (Figure S12).

Thus, the urea modification has a more pronounced effect on systems with weak (Set 1) and moderate (Set 2) internal cohesion than the β-sheet-forming PAs of Set 3. Set 4 PAs (**PA 10−13**) have the same strong β-sheet-forming region VVAA but with a shorter hydrophobic tail and two negatively charged terminal amino acids (EE). In this set, an extra **PA 12** with one more $-CH_2-$ was designed to exclude the effect of different atom numbers resulting from the urea modification. As shown in Figure S13, urea-modified **PA 13** is the only PA in Set 4 that exclusively forms long filaments at all pH values. In conclusion, these observations suggest that urea modification can help to stabilize the elongated morphology for both cationic and anionic PAs. Furthermore, it highlights the possibility of using a small urea motif to obtain an intermolecular cohesion similar to that achieved with a long peptide sequence.

https://doi.org/10.1021/acs.biomac.3c01463
Biomacromolecules 2024, 25, 2823−2837

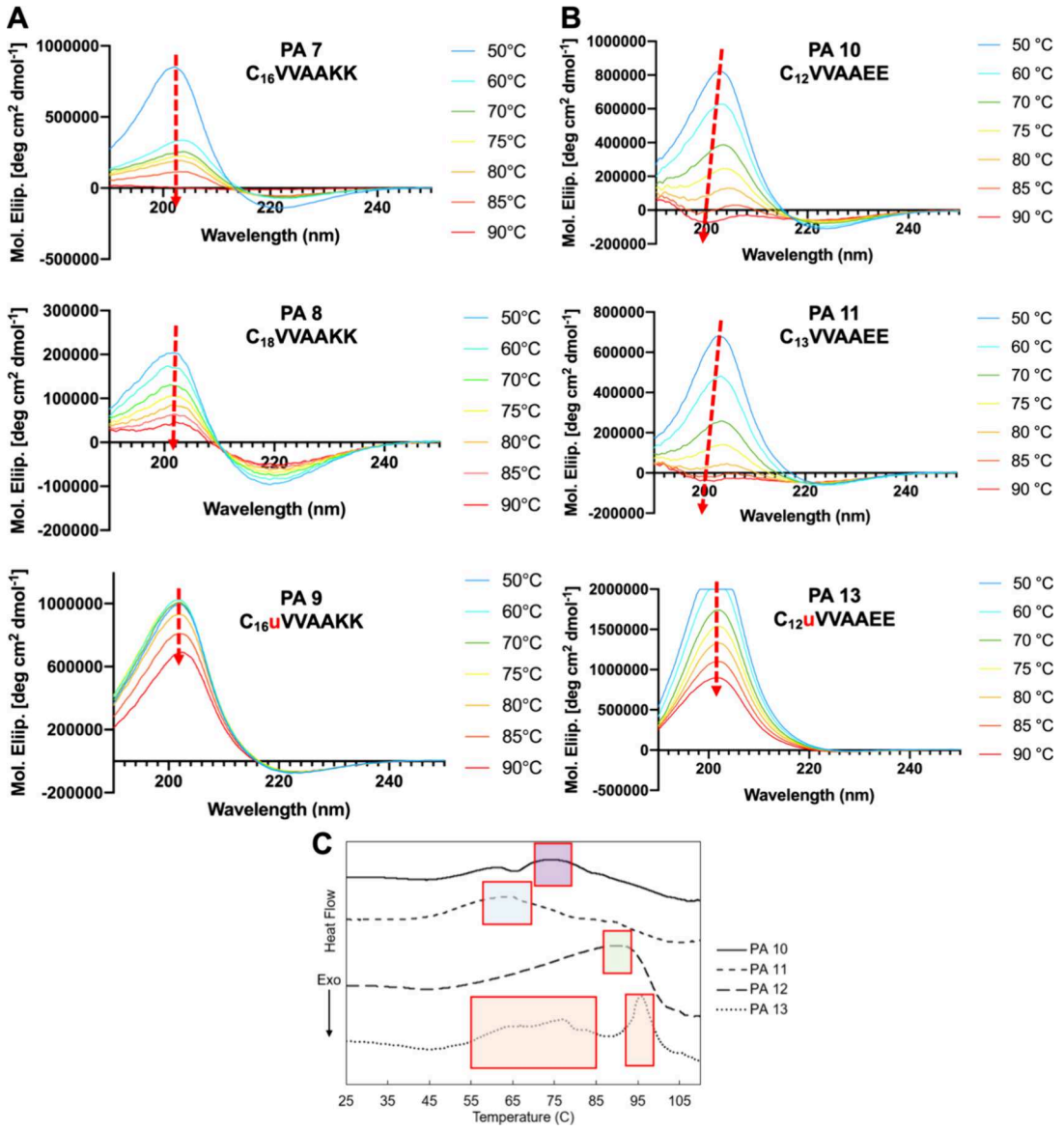

Figure 4. Solution-phase structure stability of selected PA nanostructures at various temperatures. VT-CD spectra of (A) Set 3 PAs: **PA 7**−**9**; (B) Set 4 PAs: **PAs 10, 11,** and **13**, from top to bottom, respectively. (C) NanoDSC heating curves for PA Set 4 (**PAs 10**−**13**). **PA 12** is excluded from CD due to its low solubility and thus noisy signal.

3.1.2. Internal Arrangement Transition Induced by pH Changes. Although the supramolecular morphology appears to be less sensitive to changes in pH, we hypothesize that the internal arrangement of PA molecules may be influenced by urea modification. We therefore sought to measure these changes in molecular packing using ThT, a widely used fluorescent dye that is well known to bind to amyloid fibrils allowing the quantification of amyloid-type β-sheets.[24] When ThT binds to the β-sheet-rich domain, the dye displays a strong fluorescent signal. As shown in Figure 3A, it is clear from the data that the urea-modified **PA 9** (green color) possesses the highest intensity at all pH values, while the longer tail **PA 8** (red color) is in the middle and **PA 7** (black color) exhibits the lowest intensity. The data thus indicate that the urea group enhances the fibril formation more than adding two methylene groups.

To confirm that the increased β-sheet fibril formation is related to the extra hydrogen bond from the urea, we performed FT-IR experiments on Set 3 (pH 7 in Figure 3B, and other pH values in Figure 3C). We observed here qualitatively that the urea-modified **PA 9** presents a more intense, shaper amide I peak than **PA 7** and **PA 8**, which suggests a higher amount of hydrogen bonding amides. Moreover, **PA 9** shows a shift of amide I peak toward lower frequencies, from 1621 to 1615 cm^{-1}, indicating stronger hydrogen bonding. This suggests that the urea-modified **PA 9** has a high level of molecular order and more β-sheet content due to an increase in the stability of the hydrogen bonding network throughout the PA filaments.[25] Then, we performed FT-IR for pH 1, 4, 6, and 7. The data for pH 9 are not considered here due to the overlap of the buffer signal with the amide I peak. As shown in Figure 3C, there are several trends that can be made based on the intensity and position of the amide I peak. First, a more intense signal can be found in the urea-modified **PA 9** at all pH values compared to the other PAs followed by **PA 8** and then **PA 7**, consistent with the ThT assay. Second, the amide I peak is consistently blue-shifted for **PA 9** relative to the other PAs, suggesting stronger hydrogen

https://doi.org/10.1021/acs.biomac.3c01463
Biomacromolecules 2024, 25, 2823−2837

bonding. Third, some shifting to lower frequencies can be found at low pH for all three of these PAs because charged amine groups can participate in strong hydrogen bonds. In summary, FT-IR and ThT assay data indicate that there is a stronger hydrogen bonding network and a higher level of molecular order in the urea-modified PA nanostructures from pH 1 to pH 7.

Then, we performed the ThT assay, FT-IR, and CD from pH 1 to 9 on the anionic PAs (set 4). At pH 9, where strong molecular repulsion due to fully deprotonated charged head groups is expected, **PA 10** has a very low signal at 480 nm in the ThT assay (red arrow in Figure 3D), indicating lower β-sheet content, consistent with the FT-IR (red arrow in Figure 3E) and CD spectrum (red arrow in Figure 3F). As the length of the alkyl tail increases, by one $-CH_2-$ for **PA 11**, and two $-CH_2-$ for **PA 12**, the β-sheet content also increases. For urea-modified **PA 13**, a strong signal at 480 nm in the ThT assay can be found for all pH values, while intense signals can be obtained from CD, especially for pH 6 and 9 (Figure 3I). The results from the FT-IR of Set 4 PAs are not as conclusive as those of Set 3 PAs (Lys-based). However, the urea modification still causes a blue shift of the amide I peak for the Glu-based **PA 13**, the PA that shows the most intense absorbance among the three PAs at all pH ranges (details seen in SI and Figure S14). The intensity of the signals for the Glu-based PAs may be influenced by their poor solubility, which also highlights the improved water solubility conferred by the urea modification.

In summary, urea modification plays a key role in promoting fibril formation over a wide pH range, although the sequence of the PAs also influences the tendency to form micelles or to precipitate. In the PAs with a stronger propensity toward β-sheet formation, the impact of urea modification is less pronounced. However, the β-sheet content is strengthened by this modification. Thus, the urea group allows fibril formation without increasing the peptide sequence or length of the alkyl tail, which may affect the biological properties and costs (a shorter peptide sequence will be cheaper).

3.2. Urea Modification Provides Thermal Stability to the Nanostructures. Next, we studied the effect of urea modification on the thermal stability of PA nanostructures. Since PA nanostructures are dynamic and formed by noncovalent interactions, increasing the temperature should affect the morphology of the assemblies and is expected to cause nanofiber disassembly.[2,5] This maybe a result of weakened hydrogen bonds. Our hypothesis was that the addition of the urea group may provide nanostructures that are more resistant to temperature. As shown in Figure S15, increasing temperature clearly effects the attachment of nanostructure and causes the morphology transition of Set 2 PAs. The variable temperature SAXS measurements (Figures S16 and S18) suggest the transition of fibrils to large aggregates at a high temperature. Unfortunately, the experiments do not indicate if the fibers disassembled and then aggregates were formed or if the aggregates are groups of fibers coming together. Notably, for Set 2 PAs, both AFM and SAXS data indicate that urea-modified **PA 6** has the most stable morphology at a high temperature.

We performed variable temperature CD (VT-CD) to investigate the relationship between temperature and secondary structures. This was complemented by NanoDSC for the Set 4 PAs. For these experiments, Set 3 and Set 4 PAs, which all form elongated objects at neutral pH, were chosen to avoid the effect caused by differences in the initial morphology. In the case of Set 3 PAs, VT-CD (Figure 4A) revealed that these three PAs have β-sheet structure with a maximum peak around 208 nm and a minimum peak around 220 nm. Upon heating, the CD intensity of **PA 7** and **PA 8** at the 208 nm maximum significantly decreases by around 90 and 80%, respectively. Notably, urea-modified **PA 9** has a negligible change from 50 to 75 °C followed by a slight reduction of approximately 30% from 80 to 90 °C. Based on these observations, we concluded that the secondary structure of the urea-modified **PA 9** is more stable to thermal changes. Generally, the intensity of the CD spectra for all PAs in Set 4 decreases as the temperature increases, indicating a loss of the β-sheet secondary structure (Figure 4B). However, SAXS results show that the whole set was morphologically stable between 20 and 90 °C (Figures S17 and S18). Therefore, shape features did not present significant alterations despite the changes in the secondary structure. When proteins unfold, the CD spectra can resemble a mixture of polypeptides, resulting in a net spectrum around zero with no defined peaks.[23] This can be observed for **PA 10** and **PA 11**, where temperature-induced denaturation occurs around 70−80 °C. In contrast, while urea-modified **PA 13** undergoes a limited loss of secondary structure with increasing temperature, the overall β-sheet secondary structure is maintained, and the PA nanostructure does not denature. In conclusion, CD spectra suggest that the urea modification provides sufficient intermolecular hydrogen bonding to prevent disassembly at high temperatures. As hypothesized, the extra hydrogen bond provided by urea, near the core of the PA molecules, enhances the stability of the nanostructures (the effect of hydrogen bonding near the core has been beautifully described by the group of Hartgerink[26]).

These findings were supported by NanoDSC experiments on Set 4 (**PAs 10−13**). The loss of PA solution-phase structure (denaturation) involves reduction in the magnitude of the intramolecular forces providing structural stability.[27] This is an endothermic process, shown by positive peaks in Figure 4C. **PA 10** and **11** denature at the lowest temperatures, showing endothermic transitions centered around 75 and 65 °C, respectively. The heat flow curves show a broad denaturation event consistent with the VT-CD findings of a reduction in peak intensity around 200 nm (arrows in Figure 4B) as the temperature is increased. Urea-modified **PA 13** shows a sharp endothermic structure transition close to 95 °C, indicating denaturation at a higher temperature than the range probed with VT-CD. Additionally, **PA 13** also shows a broad endothermic event between 55 and 85 °C, coinciding with a slow loss of secondary structure shown by VT-CD. Despite a loss of solution-phase structure at 95 °C, **PA 13** exhibited a higher degree of stability against increased temperatures when compared to unmodified PAs. Altogether, these results show that urea modification can increase the thermal stability of PA solution-phase structures.

3.3. Urea Modification Contributes to the Intermolecular Cohesion. All of the above observations indicate the urea modification stabilizes the nanostructures via stronger hydrogen bonding, resulting in a higher order in the molecular level. Förster resonance energy transfer (FRET) can be used to assess molecular exchange kinetics, by tracking a pair of donor and acceptor fluorophores over time.[28,29] The DiO (donor) and DiI (acceptor) were encapsulated in Set 1 PA solutions and mixed. The FRET ratio, calculated by I_{DiI}/I_{DiO}, was monitored within 4 h to assess the kinetic profile, as shown in

https://doi.org/10.1021/acs.biomac.3c01463
Biomacromolecules 2024, 25, 2823−2837

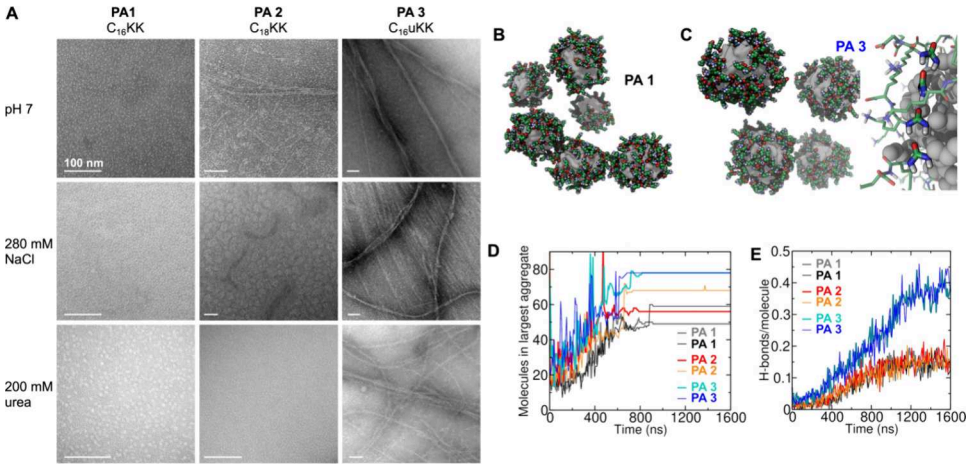

Figure 5. Morphology study of **PA 1**−**3** with the addition of salt or urea. (A) TEM images of **PA 1**−**3** nanostructures with (top row) pure water, (middle row) 280 mM NaCl, and (bottom row) 200 mM urea. Scale bar: 100 nm. PA solutions were dissolved in water, and 280 mM NaCl or 200 mM urea solution was added to the PA solutions to have a final PA concentration at 1 mg/mL. The resulting solution was annealed and aged overnight before imaging. (B) Aggregates formed in 1600 ns of MD simulation starting from 256 randomly placed **PA 1** molecules in aqueous 280 mM NaCl. (C) Aggregates formed in a similar simulation of **PA 3**. The zoomed-in image (right) shows chains of H-bonded urea groups in **PA 3** simulations. (D) Number of molecules in the largest aggregate during these simulations for each of three PAs (**PA 1**−**3**), with two replicates per PA. (E) Number of intermolecular amide/urea H-bonds per molecule in these simulations.

Figure S19. The FRET ratio for all PAs in Set 1 increased with time and reached a plateau after several hours. It is notable that **PA 2** (long alkyl tail) and **PA 3** (urea-modified) have a similar FRET ratio over time, which is lower than **PA 1**. This observation suggests that there is less molecular exchange of PAs between nanostructures, which further confirms the stabilization effect of urea modification.

Next, we attempted to decouple the influence of electrostatic repulsions (by adding 280 mM NaCl, a high salt concentration to achieve complete charge screening) and intermolecular hydrogen bonding (by adding 200 mM urea) to study how, and to what extent, the urea group can overcome the external influences that the PA assemblies may encounter. Only Set 1 and Set 2 PAs were studied as the backbone of sets 3 and 4 is stable across these conditions (as explained above). As shown in the left column of Figure 5, **PA 1** forms spherical structures independent of solution additives. **PA 2** forms elongated structures in water but transitions to spherical aggregates when salt is added (middle column of Figure 5). This is an interesting result because charge screening usually enhances supramolecular structure formation due to a reduction in charge repulsion. Meanwhile, no morphological transition is observed on **PA 3** filaments when salt is added (right column of Figure 5A). This suggests the additional hydrogen bonding of the urea results in enhanced resistance toward charge screening compared to **PA 2**. A similar trend is observed with Set 2 PAs, shown in Figure S20. After the addition of a high concentration of salt, long fibers, and worm-like micelles are seen on urea-**PA 6**. Meanwhile, a total fiber-to-micelle transition occurs with **PA 5**. These observations indicate that the urea-modified PA can better resist the influence of external forces on its morphology.

To better understand the assembly at the molecular level and confirm that the improved resistance to salt is due to the urea motif, we performed MD simulations. The formation of PA aggregates from 256 initially randomly distributed PA monomers in 280 mM NaCl solution is shown in Figure 5B−E. The systems underwent 1200 ns of simulated annealing (885 to 295 K) and were held at 295 K for an additional 400 ns. Early in the simulations (at high temperatures), most of the PA molecules are free monomers, as shown in Figure 5D. As the temperature drops below about 600 K (t > 580 ns), the PA molecules rapidly begin to coalesce into well-defined micelle-like aggregates. These aggregates become stable for temperatures below 450 K after about 450 ns. As illustrated in Figure 5B,C and quantified in Figure 5D, the urea-modified **PA 3** forms larger aggregates than the PAs lacking the urea group (**PA 1**−**2**). Although the amide-linked PA with the longer 17-carbon alkyl tail (**PA 2**) on average forms larger aggregates than that with a 15-carbon alkyl tail (**PA 2**), these aggregates are smaller than those formed by **PA 3**, which has a urea group and a 16-carbon alkyl tail. The peptide backbones of **PA 3** also tend to align owing to the strong hydrogen bonds elicited by the urea group (Figure 5C, right), while **PA 1** and **PA 2**, which have amide groups only, show no such tendency. Indeed, we found more than *twice* as many backbone intermolecular hydrogen bonds per molecule in the **PA 3** aggregates than in aggregates of **PA 1** or **PA 2** (Figure 5E). These experimental and theoretical observations suggest that strengthened intermolecular hydrogen-bonding interactions stabilize the nanostructures against aggregation when repulsion is screened by ions.

Free urea destabilizes proteins by forming hydrogen bonds with them[30] and changing bulk water−water interactions, resulting in a decrease in protein hydration.[31] Thus, we added 200 mM urea solution to the PAs and performed TEM at neutral pH to assess if the urea-modified PA can resist the unfolding effect. As shown in the last row of Figure 5A, **PA 1** keeps its micelle shape, while **PA 2** undergoes a fiber−micelle transition. The urea breaks the hydrogen bonds between PAs and exhibits a similar effect to that observed with salt. Similar observations were seen in **PA 4** and **PA 5** (Figure S20). The transition from amorphous aggregates and fibers to uniform spherical micelles can be more clearly observed in Set 2. Meanwhile, the urea-modified PAs (**PA 3** and **PA 6**) kept their elongated shape (Figure 5A and last row of Figure S20). The stabilization effect of the urea modification is more prominent in **PA 3** than in **PA 6**, which shows a decrease in fiber length.

https://doi.org/10.1021/acs.biomac.3c01463
Biomacromolecules 2024, 25, 2823−2837

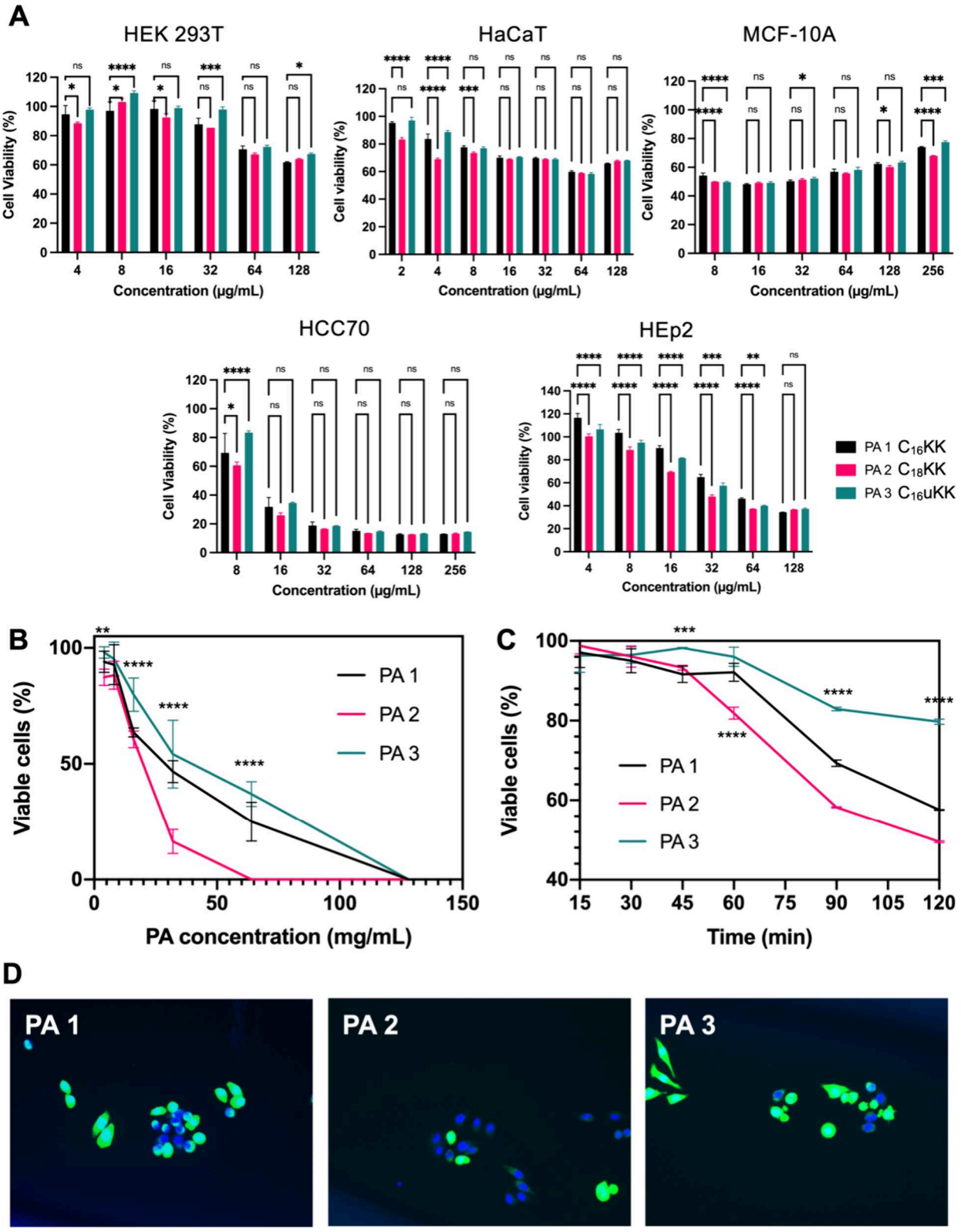

Figure 6. Cytotoxicity of **PA 1**−**3** toward various cells. (A) XTT assay of HEK-293T, HaCaT, MCF-10A, HCC 70, and HEp2 cell lines, respectively, with 24 h of treatment. (B) Quantification of HEp2 cells (62−209 cells were counted for each plate) 3 h after treatment with various concentrations of PA assemblies. (C) Quantification of HEp2 cells after treating with PAs at 32 μg/mL at various time spots of 15, 30, 60, 90, 120 min. Black line indicates **PA 1**, red line indicates **PA 2**, and green line indicates **PA 3**. (D) Live (green) and nuclei (blue) staining of HEp2 cells treated with PA assemblies at 32 μg/mL for 2 h. Data in A, B, and C (n = 3 biological replicates) are mean ± s.d.; two-way ANOVA, ****P < 0.0001.

https://doi.org/10.1021/acs.biomac.3c01463
Biomacromolecules 2024, 25, 2823−2837

This most likely relates to the differences in the size of the lipid and peptide segments; the urea has a stronger effect when they are shorter (when compared to each other). Second, the longer adjacent alkyl tail in Set 1 packs PAs more tightly, assisting the urea motif to optimize the hydrogen bond for further aggregation (of course, changes in hydration may not be discarded). In conclusion, these observations suggest that urea-induced denaturation can be eliminated to some degree when more intermolecular hydrogen bonds exist. Importantly, the addition of external urea molecules is not able to disturb these hydrogen bonds completely, which we attributed to being a consequence of the proximity of the urea motif to the core.

3.4. Urea Modification Affects the PA−Membrane Interaction. It is well-known that the interaction between cationic PAs and biological membrane can play a critical role in antimicrobial and anticancer activity,[10,32] though the detailed mechanisms are still not fully understood. This membrane-targeted mechanism is complicated by the diversity of peptide sequences and structures of antimicrobial amphiphiles.[33] However, the morphology (micelle, short fiber, and longer fiber)[6,9] and cohesion/stability of nanostructures[7] have been reported to be the decisive factors. Herein, we studied if the urea modification can have an impact on the PA−membrane interactions in both mammalian cells and bacteria. Only sets 1−3 were selected for the biological assays due to the specific interaction between their positively charged head groups and biological membranes.

First, we assessed the effect of the cell culture media (e.g., proteins and salts) on the morphologies of PA assemblies. The three sets of cationic PAs were incubated with HEp2 cell medium (final concentration of 100 μg/mL) for 2 h at 37 °C. A clear disruption of elongated objects by cell media can be found with Set 1−3 PAs, while little differences can be observed between them. As shown in the first row in Figure S21A, all PAs in Set 1 formed micelles or aggregates, while the urea-modified **PA 3** showed a dendritic arrangement of uniform micelles (the morphologies may be affected by drying or molecules present in the media). In addition, the sizes of micelles formed by the urea-modified **PA 3** are more uniform and larger (Figure S21B) than those of the other two PAs. The difference in size and distribution may be due to 1) the fact that the urea motif stabilizes the balance among molecular interactions to form uniform-size nanostructures, and 2) urea hydrogen bonds allow the presence of more PA molecules within a nanostructure. Therefore, **PA 3** could be a potential nanocarrier with a controlled release rate (two steps of release: fibril−micelle transition and micelle disassembly) and enhanced drug loading capacity (fibril shape). There is little difference among the PAs in the other two sets, which confirms that the urea modification has a greater effect on PAs with a smaller peptide portion. Set 2 PAs form aggregates (middle row in Figure S21A), and Set 3 PAs form uniform elongated objects (last row in Figure S21A). Furthermore, the morphological and chemical stability of the PA's nanostructures was determined after 2 h of incubation in human serum (see Figure S22). Among Set 1 PAs, only the urea-modified **PA 3** was able to maintain the fibril morphology (see Figure S22A). The HPLC, combined with MALDI, indicated that all Set 1 PAs had over 80% remaining PA molecules after incubation with serum. However, **PA 3** is less stable than **PA 1** and **PA 2**, possibly due to the increased interaction between the urea motif and serum components such as lipoproteins and fats. Additionally, urea-modified **PA 6** and **PA 9** were found to maintain their fibril nanostructures in serum solution, further supporting the conclusion that urea modification enhances intermolecular cohesion and stabilizes the nanostructures.

3.4.1. Urea Modification Reduces Cell Cytotoxicity. We studied the cytotoxicity of these three sets of PAs toward various cell lines. HaCaT (human keratinocyte cells), HEK-293T (human embryonic kidney cells), HEp-2 (human epithelial cancer cells), MCF-10A (human breast cells), and HCC70 (human breast cancer cells) were used in the assays. As shown in Figure 6A, Set 1 possess high toxicity toward the cancer cells HEp2 (LC_{50} < 64 μg/mL) and HCC70 (LC_{50} < 16 μg/mL), while presenting moderate cytotoxicity to HEK 293T, HaCaT, and MCF-10A cells. Selective cytotoxicity of cationic amphiphiles for cancer cells over normal cells has been reported[34] and is likely due to the more acidic membranes present in cancer cells.[35] Meanwhile, the other two sets of PAs do not exhibit significant toxicity to cells (data shown in Figure S23A,B). Interestingly, Set 2 (Figure S23A,B) is less toxic than Set 1 although they have a similar spherical morphology in cell culture media (second row of Figure S21) and the same amount of lysine residues. A possible reason for the reduced toxicity of Set 2 PAs might be their shorter alkyl tail,[36] which limits their ability to insert into cell membranes (Table S3). Set 3 (Figure S23C) does not present toxicity toward HEp2 cells up to a concentration of 256 μg/mL, although they have the same length of alkyl tail as Set 1 PAs and higher hydrophobicity than Set 2 PAs. In this case, the negligible cytotoxicity possibly because of their elongated morphology[9] in cell media (third row of Figure S21) and strong intermolecular cohesion.[7]

It is worth noting that for the normal human cell lines (HEK 293T, HaCaT, and MCF-10A), **PA 2** (with a "longer" tail), and the urea-modified **PA 3** presented the highest cell viability, especially at relatively low concentrations. This maybe a result of the stronger molecular cohesion contributed by H-bonds and hydrophobic collapse, which makes the PAs more difficult to disassemble and interact with the cytoplasm membranes.[3,7]

To further study the differences in the killing behavior between the urea-PA and unmodified PAs, Set 1 was selected to perform a live/dead assay on the HEp2 cell line. A low cell density of 1×10^4 was used to avoid cell−cell interaction. The cells were stained by Hoechst (nuclei, blue) and calcein AM (live, green) followed by treating with PA solutions. The cell viability in dose−response were studied from 2 to 128 μg/mL PA concentration, as shown in Figure 6B. **PA 2** (red line) shows the highest toxicity at all concentration, while **PA 1** (black line) and **PA 3** (urea-modified, green line) have similar cytotoxicity. These data show the same tendency but higher cytotoxicity, when compared to the XTT assay, due to the rapid calcein leakage from the dead cells and damaged plasma membranes, suggesting membrane targeting as the mode of action. Then, the quantification of viable cells at 32 μg/mL was assessed at various time points to obtain a more detailed killing time of the three PAs on the Set (Figure 6C, and detailed images can be found in Figures S25−S27). A rapid killing within 2 h, visualization of stained cells shown in Figure 6D, can be observed with all PAs. The viability of cells starts to decrease after 45 min (**PA 2**) and 60 min (**PA 1** and **PA 3**) treatment, while the cell viability keeps the same order: **PA 3** > **PA 1** > **PA 2**. In conclusion, urea-**PA 3** has the least cytotoxicity at various concentrations and time points. The urea hydrogen bonds increase the cohesion, which hinders the

https://doi.org/10.1021/acs.biomac.3c01463
Biomacromolecules 2024, 25, 2823−2837

A

MIC (μg/mL)	PA 1 C_{16}KK	PA 2 C_{18}KK	PA 3 C_{16}uKK	PA 4 C_{12}VGAGKK	PA 5 C_{14}VGAGKK	PA 6 C_{12}uVGAGKK	PA 7 C_{16}VVAAKK	PA 8 C_{18}VVAAKK	PA 9 C_{16}uVVAAKK
MRSA JE2	64	16 (MBC 64)	32 (MBC 64)	>256	256	256	>256	>256	>256
A. baumannii	32	16	32 (MBC 64)	256	64	128	>256	>256	>256

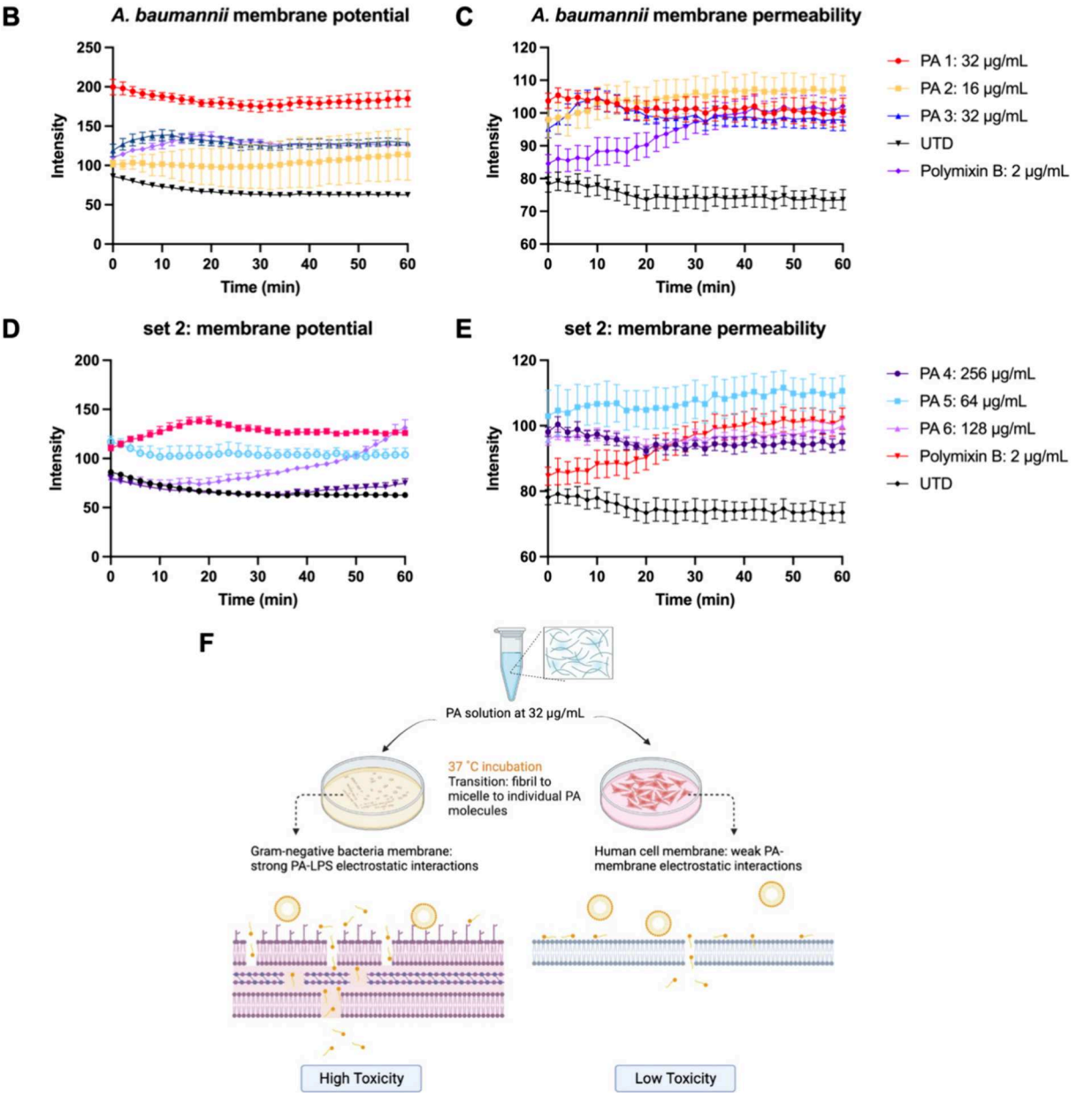

Figure 7. Microbiological studies of PAs. (A) MIC and MBC (in brackets) of PA nanostructures in μg/mL against *S. aureus* JE2 and *A. baumannii*. (B, D) Cytoplasmic depolarization assay done at 0.3 McFarland unit. Intensity of DiSC3(5) with untreated, **PA 1−3**, **PA 4−6**, and polymyxin B at MIC value for 60 min was measured (2 min interval). (C, E) Membrane permeability assay. Fluorescence intensity of PI with untreated **PA 1−3**, **PA 4−6**, and polymyxin B at MIC value for 60 min was measured (2 min interval). (F) Schematic description of urea-modified **PA 3**'s selectivity between bacteria and human cell line.

disassembly of nanostructures surrounding cells and minimizes membrane disruption by the PAs.

3.4.2. Urea Modification Increases the Affinity to Bacteria Membrane. Studies have demonstrated that cationic PAs exhibit antimicrobial activity by physically disrupting bacterial membranes.[37] Our theory is that the process involves two steps. First, PA nanostructures with a positive surface charge interact electrostatically with the negatively charged bacterial membrane, which leads to the disassembly of PA nanostructures. Second, the hydrophobic tail of PA inserts into the bacterial membrane through hydrophobic collapse. Therefore, we believe the antimicrobial efficacy of cationic PAs strongly correlates with their ability to attach and disrupt the bacterial membrane. This process is influenced by the interplay between

https://doi.org/10.1021/acs.biomac.3c01463
Biomacromolecules 2024, 25, 2823−2837

the cationic surface charge, the hydrophobicity, and the internal cohesion of the PA assemblies.[38,39] We tested the antimicrobial activity of the cationic PAs against *Staphylococcus aureus* JE2 (a Gram-positive organism) and *Acinetobacter baumannii* (a Gram-negative organism) to study whether the urea modification could affect the PA−bacterial membrane interaction. The MIC and MBC are shown in Figure 7A. Set 1 PAs possessed an MIC ≤ 64 μg/mL against both *S. aureus* and *A. baumannii*. Set 2 and, especially, Set 3 PAs did not exhibit considerable toxicity to bacteria. The low toxicity toward bacteria of Set 2 and Set 3 may be due to the short alkyl tail (though there is no simply linear relation between hydrophobicity and antimicrobial activity) and their fibril morphology. For these six PAs, the electrostatic interaction between the charged PA head (optimal range +4 to +6)[40] and lipopolysaccharides (LPS) is probably not sufficient to cause bacterial death.

Another noteworthy point is the MBC for Set 1. For **PA 3**, the ratio of MBC to MIC for both strains is 2, indicating bactericidal activity. This value does not change for both strains up to 10^8 CFU/mL bacteria density (SEM image in Figure S28), which shows the absence of inoculum effect at a high bacteria load.[41] However, the **PA 1** is a bacteriostatic antibiotic to both strains and **PA 2** is bactericidal only for *S. aureus* (MBC/MIC = 4). Thus, a more efficient cell-killing mechanism of the urea-modified PAs can be proposed as the reason for this observation. It has been reported that multiple hydrogen bonding interactions due to the urea motif can occur with bacterial membrane[42] resulting on antibacterial effects.[43] Cationic peptides can accumulate on bacterial membranes due to electrostatic attractions, and the affinity to membrane may be further strengthened by the hydrogen bonds between molecules and lipid membranes.[14] In contrast, the zwitterionic character of mammalian membranes (relative to bacteria) results in reduced electrostatic attraction.[14] Thus, it is important to note that urea−PA has the potential for greater selectivity (relative lower cellular cytotoxicity described above) while possessing antimicrobial activity. In the case of HEp2, the LD50/MIC ratio of urea-modified **PA 3** is 1.5 times more than **PA 1**. In other words, a higher therapeutic index is present on the urea PA, which may translate to a better antimicrobial therapy compared with its unmodified PA analog.

As pointed out, the mode of action of urea-modified **PA 3** seems to be different than the other two, although all PAs target the bacteria membrane. To further understand the PA−membrane interactions, the membrane permeabilities and potentials of *A. baumannii* (outer and inner membrane) were studied.[44] 3,3-Dipropyl-thisdicarbocyanine (DiSC3(5)) is a dye commonly used to study the membrane potential. Fluorescence quenching occurs when the dyes accumulate within the polarized membrane, and dequenching happens when the membrane is depolarized.[45] Moreover, the membrane permeability was detected by membrane impermeable fluorescent dye PI, which stains the cell nuclei when the membrane integrity is compromised, or pores are formed.[46]

As seen in Figure 7B, at the MIC value, all Set 1 PAs have a higher fluorescence intensity than the untreated sample, which means rapid dissipation of the membrane potential. The order of intensity (**PA 1** ≫ **PA 3** ∼ polymyxin B > **PA 2**) matches the measured zeta potential order. Furthermore, as shown in Figure 7C, all PAs in Set 1 show good ability to increase the bacteria membrane permeability (no significant difference among samples), and the action is rapid compared to polymyxin B in the first 30 min. Therefore, the alteration of the bacteria membrane potential (surface charge) plays a crucial role in the antimicrobial activity of **PA 1**. For **PA 2** and **PA 3**, influences on both the membrane potential and the permeability are imperative for their antimicrobial efficacy. AFM images (Figure S29) indicated that the bacterial surface exhibited roughness (multiple sharp peaks in the height profiles) after being treated with **PA 1−3** for 2 h. These observations confirmed the membrane-targeting killing mechanism of our PAs. The same experiments were performed with Set 2 PAs, and a similar permeability result was achieved (Figure 7E), confirming the membrane-penetrating ability of these PAs. A minor change of membrane potential with Set 2 was found (Figure 7D), which is expected due to their low cationic character (indicated by the zeta potential). However, urea−**PA 6** depolarizes the bacteria membrane after 1 h of treatment (shown in light purple), similar to polymyxin B (Set 1 PAs as well). This might hint that the urea hydrogen bonds assist in the PA nanostructure−membrane attachment step and that urea−Mg^{2+} interaction may also play a role.

Overall, the cell and bacteria assays suggest that urea modification may offer several advantages in biological application. First, there is typically an inverse relationship between the selectivity for bacterial membranes and peptide hydrophobicity due to the increased affinity with zwitterionic phospholipids.[47] The urea modification can alter the optimum hydrophobicity window to maintain the selectivity. Second, urea hydrogen bonding can enhance the affinity of PA to bacteria membrane, which may subsequently increase the antimicrobial activity of the PA.

4. CONCLUSIONS

In summary, this work provides a new strategy to enhance the stability of amphiphilic supramolecular nanostructures against external stimuli by conjugating a urea motif between the hydrophobic and hydrophilic portions. Microscopy studies and SAXS revealed the stabilization role of urea modification to PA-elongated objects in response to pH changes. Additionally, we showed that the urea modification is better suited at stabilizing PA structures than adding a $-C_2H_4-$ to the hydrophobic tail. CD and ThT studies further demonstrated that urea aids in maintaining the β-sheet secondary structure and the fibril morphology against pH influence. Moreover, a stabilization effect to high temperature was found by VT-CD and NanoDSC. The intermolecular urea hydrogen bonds can overcome the disruption caused by counterions and denaturation agents (free urea molecule). From these four sets of PAs in our study, it can be concluded that, in most cases, the efficacy is inversely proportional to the original stability of PA nanostructures.

Finally, we found that the urea-modified PA has different behaviors when interacting with cell/bacteria membranes than their unmodified PA counterparts, showing an increase in the selectivity between cells and bacteria and a bactericidal function. We attribute this behavior to the enhanced attachment of the PA−membrane through urea hydrogen bonds. Importantly, compared to the PA having a longer alkyl tail, with the urea modification, the cytotoxicity of PA assemblies can be reduced and the stability toward external stimuli can be increased. Thus, our study provides a specific chemical modification that can be easily applied to many self-

https://doi.org/10.1021/acs.biomac.3c01463
Biomacromolecules 2024, 25, 2823−2837

assembled biomaterial systems, with less impact on the original molecule design (biological function) and increased stability.

■ ASSOCIATED CONTENT

Supporting Information

The Supporting Information is available free of charge at https://pubs.acs.org/doi/10.1021/acs.biomac.3c01463.

PA chemical structures, mass spectra, HPLC chromatograms, and H NMR spectrum; TEM images of **PA 1−3** at pH 7.4; AFM images of **PA 1−3** at pH 1, 6, and 9; cryo-EM images of **PA 1−3** at pH 6; SAXS modeling of PAs prepared at different pHs; TEM and AFM images of 4−9 at pH 1, 6, and 9; TEM images of **PA 10−13** at pH 1, 6, and 9; FT-IR spectrum of **PA 10−13** at pH 1, 4, 6, and 7; VT-AFM images of **PA 4−6**; VT-SAXS plots of **PA 4−9**; FRET assay of **PA 1−3**; dynamic simulation methods; TEM images of **PA 4−6** prepared with NaCl and urea solution; TEM images and width measurement of **PA 1−9** incubated with cell media for 2 h; cytotoxicity assay of **PA 4−9** toward HEp2 and HaCaT cell lines; AFM and height profile of **PA 1−3**-treated bacteria; zeta potential and calculated log*P* value of **PA 1−9**; live/dead images of **PA 1−3** at 32 μg/mL; and SEM images of *MRSA* JE2 treated with **PA 1** overnight (PDF)

■ AUTHOR INFORMATION

Corresponding Author

Martin Conda-Sheridan − *College of Pharmacy, University of Nebraska Medical Center, Omaha, Nebraska 68198, United States;* orcid.org/0000-0002-3568-2545; Phone: +1 402-559-9361; Email: martin.condasheridan@unmc.edu

Authors

Huihua Xing − *College of Pharmacy, University of Nebraska Medical Center, Omaha, Nebraska 68198, United States;* Present Address: Alfred E. Mann Department of Biomedical Engineering, University of Southern California, Los Angeles, California 90089, United States

Caleb Wigham − *Department of Chemical & Biological Engineering, Center for Biotechnology and Interdisciplinary Studies, Rensselaer Polytechnic Institute, Troy, New York 12180, United States*

Sieun Ruth Lee − *Department of Materials Science & Engineering, Chemistry, Biomedical Engineering, Medicine, and Simpson Querrey Institute, Northwestern University, Evanston, Illinois 60208, United States;* orcid.org/0000-0002-6835-0248

Aramis J. Pereira − *College of Pharmacy, University of Nebraska Medical Center, Omaha, Nebraska 68198, United States*

Luana J. de Campos − *College of Pharmacy, University of Nebraska Medical Center, Omaha, Nebraska 68198, United States*

Agustín S. Picco − *Instituto de Investigaciones Fisicoquímicas Teóricas y Aplicadas, INIFTA-CONICET-UNLP, La Plata 1900, Argentina;* orcid.org/0000-0003-4683-7319

Cristián Huck-Iriart − *ALBA Synchrotron Light Source, Experiments Division, 08290 Cerdanyola del Vallès, Spain;* Present Address: ALBA Synchrotron Light Source, Carrer de la Llum 2−26, Cerdanyola del Vallès, 08290 Barcelona, Spain.; orcid.org/0000-0001-5734-2499

Carlos Escudero − *ALBA Synchrotron Light Source, Experiments Division, 08290 Cerdanyola del Vallès, Spain;* orcid.org/0000-0001-8716-9391

Laura Perez-Chirinos − *Center for Cooperative Research in Biomaterials (CIC biomaGUNE), Basque Research and Technology Alliance (BRTA), Donostia 20014 San Sebastián, Spain*

Sandun Gajaweera − *Department of Anatomy and Physiology, Kansas State University, Manhattan, Kansas 66506, United States*

Jeffrey Comer − *Department of Anatomy and Physiology, Kansas State University, Manhattan, Kansas 66506, United States;* orcid.org/0000-0003-4437-1260

Ivan R. Sasselli − *Center for Cooperative Research in Biomaterials (CIC biomaGUNE), Basque Research and Technology Alliance (BRTA), Donostia 20014 San Sebastián, Spain; Centro de Fisica de Materiales (CFM), CSIC-UPV/EHU, Donostia 20018 San Sebastián, Spain;* orcid.org/0000-0001-6062-2440

Samuel I. Stupp − *Department of Materials Science & Engineering, Chemistry, Biomedical Engineering, Medicine, and Simpson Querrey Institute, Northwestern University, Evanston, Illinois 60208, United States;* orcid.org/0000-0002-5491-7442

R. Helen Zha − *Department of Chemical & Biological Engineering, Center for Biotechnology and Interdisciplinary Studies, Rensselaer Polytechnic Institute, Troy, New York 12180, United States;* orcid.org/0000-0002-0766-5705

Complete contact information is available at: https://pubs.acs.org/10.1021/acs.biomac.3c01463

Author Contributions

M.C.-S. conceived the idea, supervised the experiments, funded the project, and performed data analysis; H.X. performed PA synthesis, samples preparation, CD, TEM, AFM, SAXS, ThT, cell, and bacterial experiments; C.E. performed SAXS experiments; C.H.-I. and A.S.P. analyzed SAXS and contributed to the overall idea; C.W. and R.H.Z. suggested experiments, performed, and analyzed the DSC experiment; S.R.L. performed cryo-TEM; L.P.-C. and I.R.S. performed and analyzed the FT-IR experiments; L.C. and A.P. performed the NMR, stability of PAs in serum, and sample preparation for bacteria imaging by AFM; S.I.S. provided scientific suggestions. The manuscript was written with contributions and feedback from all authors. All authors have given approval to the final version of the manuscript.

Funding

MC-S thanks the support of the National Science Foundation (NSF), CAREER Award DMR-1941731. RHZ and CW acknowledge the support of the NSF, CAREER Award DMR-2045510. IRS acknowledges financial support from Maria de Maeztu Unit of Excellence (MDM-2017-0720), Gipuzkoa Foru Aldundia (Gipuzkoa Fellows Program, Diputacion Foral de Gipuzkoa: 2019-FELL-000017-01), Ramon y Cajal Program (RYC2021-033294-I), and Spanish State Research Agency (PID2022-136392NA-I00).

Notes

The authors declare no competing financial interest.

■ ACKNOWLEDGMENTS

We want to give special thanks to Dr. Liam Palmer for editing the manuscript and for scientific feedback. HX thanks for the

support from an UNMC fellowship. The authors further acknowledge the Electron Microscopy Core Facility (Tom Bargar and Nicholas Conoan) and Nanoimaging Core Facility (Alexander Lushnikov) at UNMC for experimental assistance. SAXS measurements were also performed at the NCD-SWEET beamline at the ALBA synchrotron (project ID: 2020024345). In addition, preliminary SAXS experiments were performed at the SAXS-1 beamline of the Brazilian Synchrotron Light Laboratory (LNLS-CNPEM, Campinas, Brazil; proposal SAXS-1 20190212). A.S.P and C.H.I are staff members of CONICET and acknowledge its support. A.S.P acknowledges UNLP and C.H.I UNSAM for their support. The FT-IR measurements were performed at the Center for Cooperative Research in Biomaterials CIC biomaGUNE under the Maria de Maeztu Units of Excellence Programme − Grant MDM-2017-0720 and Grant PRE2019-090076 funded by MCIN/AEI/10.13039/501100011033 and "ESF Investing in your future" and supported by Spanish State Training Subprogramme PRE2019-090076. IRS acknowledges financial support from Gipuzkoa Foru Aldundia (Gipuzkoa Fellows Program, Diputacion Foral de Gipuzkoa: 2019-FELL-000017-01) and Ramon y Cajal Program (RYC2021-033294-I). The Cryo-EM studies were supported by the U.S. Department of Energy (DOE), Office of Science, Basic Energy Sciences, under award no. DE-SC0020884

REFERENCES

(1) Hendricks, M. P.; Sato, K.; Palmer, L. C.; Stupp, S. I. Supramolecular Assembly of Peptide Amphiphiles. *Acc. Chem. Res.* **2017**, *50* (10), 2440−2448.

(2) Ozkan, A. D.; Tekinay, A. B.; Guler, M. O.; Tekin, E. D. Effects of temperature, pH and counterions on the stability of peptide amphiphile nanofiber structures. *RSC Adv.* **2016**, *6* (106), 104201−104214.

(3) Lu, S.; Cui, W.; Li, J.; Sheng, Y.; Chen, P. Functional Control of Peptide Amphiphile Assemblies via Modulating Internal Cohesion and Surface Chemistry Switch. *Chem. - Eur. J.* **2018**, *24*, 13931.

(4) Fukushima, K.; Tan, J. P. K.; Korevaar, P. A.; Yang, Y. Y.; Pitera, J.; Nelson, A.; Maune, H.; Coady, D. J.; Frommer, J. E.; Engler, A. C.; Huang, Y.; Xu, K.; Ji, Z.; Qiao, Y.; Fan, W.; Li, L.; Wiradharma, N.; Meijer, E. W.; Hedrick, J. L. Broad-Spectrum Antimicrobial Supramolecular Assemblies with Distinctive Size and Shape. *ACS Nano* **2012**, *6* (10), 9191−9199.

(5) Tantakitti, F.; Boekhoven, J.; Wang, X.; Kazantsev, R. V.; Yu, T.; Li, J.; Zhuang, E.; Zandi, R.; Ortony, J. H.; Newcomb, C. J.; Palmer, L. C.; Shekhawat, G. S.; de la Cruz, M. O.; Schatz, G. C.; Stupp, S. I. Energy landscapes and functions of supramolecular systems. *Nat. Mater.* **2016**, *15* (4), 469−476.

(6) Milanesi, L.; Sheynis, T.; Xue, W.-F.; Orlova, E. V.; Hellewell, A. L.; Jelinek, R.; Hewitt, E. W.; Radford, S. E.; Saibil, H. R. Direct three-dimensional visualization of membrane disruption by amyloid fibrils. *Proc. Natl. Acad. Sci. U. S. A.* **2012**, *109* (50), 20455−20460.

(7) Newcomb, C. J.; Sur, S.; Ortony, J. H.; Lee, O.-S.; Matson, J. B.; Boekhoven, J.; Yu, J. M.; Schatz, G. C.; Stupp, S. I. Cell death versus cell survival instructed by supramolecular cohesion of nanostructures. *Nat. Commun.* **2014**, *5* (1), 3321.

(8) Meijer, J. T.; Roeters, M.; Viola, V.; Löwik, D. W. P. M.; Vriend, G.; van Hest, J. C. M. Stabilization of Peptide Fibrils by Hydrophobic Interaction. *Langmuir* **2007**, *23* (4), 2058−2063.

(9) Sato, K.; Ji, W.; Palmer, L. C.; Weber, B.; Barz, M.; Stupp, S. I. Programmable Assembly of Peptide Amphiphile via Noncovalent-to-Covalent Bond Conversion. *J. Am. Chem. Soc.* **2017**, *139* (26), 8995−9000.

(10) Habault, J.; Poyet, J.-L. Recent Advances in Cell Penetrating Peptide-Based Anticancer Therapies. *Molecules* **2019**, *24* (5), 927.

(11) Zasloff, M. Antimicrobial peptides of multicellular organisms. *Nature* **2002**, *415* (6870), 389−395.

(12) Xing, H.; Chin, S. M.; Udumula, V. R.; Krishnaiah, M.; Rodrigues de Almeida, N.; Huck-Iriart, C.; Picco, A. S.; Lee, S. R.; Zaldivar, G.; Jackson, K. A.; Tagliazucchi, M.; Stupp, S. I.; Conda-Sheridan, M. Control of Peptide Amphiphile Supramolecular Nanostructures by Isosteric Replacements. *Biomacromolecules* **2021**, *22* (8), 3274−3283.

(13) Gao, C.; Li, H.; Li, Y.; Kewalramani, S.; Palmer, L. C.; Dravid, V. P.; Stupp, S. I.; Olvera de la Cruz, M.; Bedzyk, M. J. Electrostatic Control of Polymorphism in Charged Amphiphile Assemblies. *J. Phys. Chem. B* **2017**, *121* (7), 1623−1628.

(14) Li, J.; Liu, S.; Lakshminarayanan, R.; Bai, Y.; Pervushin, K.; Verma, C.; Beuerman, R. W. Molecular simulations suggest how a branched antimicrobial peptide perturbs a bacterial membrane and enhances permeability. *BBA Libr.* **2013**, *1828* (3), 1112−1121.

(15) Pisárčik, M.; Pupák, M.; Devínsky, F.; Almásy, L.; Tian, Q.; Bukovský, M. Urea-based gemini surfactants: Synthesis, aggregation behaviour and biological activity. *Colloids Surf. A: Physicochem. Eng. Asp* **2016**, *497*, 385−396.

(16) Xing, H.; Rodger, A.; Comer, J.; Picco, A. S.; Huck-Iriart, C.; Ezell, E. L.; Conda-Sheridan, M. Urea-Modified Self-Assembling Peptide Amphiphiles That Form Well-Defined Nanostructures and Hydrogels for Biomedical Applications. *ACS Appl. Bio Mater.* **2022**, *5*, 4599−4610.

(17) Ashiotis, G.; Deschildre, A.; Nawaz, Z.; Wright, J. P.; Karkoulis, D.; Picca, F. E.; Kieffer, J. The fast azimuthal integration Python library: pyFAI. *J. Appl. Crystallogr.* **2015**, *48*, 510−519.

(18) Humphrey, W.; Dalke, A.; Schulten, K. VMD: visual molecular dynamics. *J. Mol. Graph* **1996**, *14* (1), 33−8. 27−8

(19) Martinez, L.; Andrade, R.; Birgin, E. G.; Martinez, J. M. PACKMOL: a package for building initial configurations for molecular dynamics simulations. *J. Comput. Chem.* **2009**, *30* (13), 2157−64.

(20) Schmit, J. D.; Kariyawasam, N. L.; Needham, V.; Smith, P. E. SLTCAP: A Simple Method for Calculating the Number of Ions Needed for MD Simulation. *J. Chem. Theory Comput.* **2018**, *14* (4), 1823−1827.

(21) Hammouda, B. A new Guinier−Porod model. *J. Appl. Crystallogr.* **2010**, *43*, 716−719.

(22) Yang, Y.; Liao, S.; Luo, Z.; Qi, R.; Mac Fhionnlaoich, N.; Stellacci, F.; Guldin, S. Comparative characterisation of non-monodisperse gold nanoparticle populations by X-ray scattering and electron microscopy. *Nanoscale* **2020**, *12* (22), 12007−12013.

(23) Pabisch, S.; Feichtenschlager, B.; Kickelbick, G.; Peterlik, H. Effect of interparticle interactions on size determination of zirconia and silica based systems − A comparison of SAXS, DLS, BET, XRD and TEM. *Chem. Phys. Lett.* **2012**, *521*, 91−97.

(24) Ortony, J. H.; Newcomb, C. J.; Matson, J. B.; Palmer, L. C.; Doan, P. E.; Hoffman, B. M.; Stupp, S. I. Internal dynamics of a supramolecular nanofibre. *Nat. Mater.* **2014**, *13* (8), 812−816.

(25) Godbe, J. M.; Freeman, R.; Lewis, J. A.; Sasselli, I. R.; Sangji, M. H.; Stupp, S. I. Hydrogen Bonding Stiffens Peptide Amphiphile Supramolecular Filaments by Aza-Glycine Residues. *Acta Biomater.* **2021**, *135*, 87−99.

(26) Paramonov, S. E.; Jun, H.-W.; Hartgerink, J. D. Self-Assembly of Peptide−Amphiphile Nanofibers: The Roles of Hydrogen Bonding and Amphiphilic Packing. *J. Am. Chem. Soc.* **2006**, *128* (22), 7291−7298.

(27) Fitzsimons, S. M.; Mulvihill, D. M.; Morris, E. R. Denaturation and aggregation processes in thermal gelation of whey proteins resolved by differential scanning calorimetry. *Food Hydrocoll.* **2007**, *21* (4), 638−644.

(28) da Silva, R. M. P.; van der Zwaag, D.; Albertazzi, L.; Lee, S. S.; Meijer, E. W.; Stupp, S. I. Super-resolution microscopy reveals structural diversity in molecular exchange among peptide amphiphile nanofibres. *Nat. Commun.* **2016**, *7* (1), 11561.

https://doi.org/10.1021/acs.biomac.3c01463
Biomacromolecules 2024, 25, 2823−2837

(29) Rajangam, K.; Arnold, M. S.; Rocco, M. A.; Stupp, S. I. Peptide amphiphile nanostructure-heparin interactions and their relationship to bioactivity. *Biomaterials* **2008**, *29* (23), 3298−305.
(30) Goyal, S.; Chattopadhyay, A.; Kasavajhala, K.; Priyakumar, U. D. Role of Urea−Aromatic Stacking Interactions in Stabilizing the Aromatic Residues of the Protein in Urea-Induced Denatured State. *J. Am. Chem. Soc.* **2017**, *139* (42), 14931−14946.
(31) Daidone, I.; Ulmschneider, M. B.; Di Nola, A.; Amadei, A.; Smith, J. C. Dehydration-driven solvent exposure of hydrophobic surfaces as a driving force in peptide folding. *Proc. Natl. Acad. Sci. U.S.A.* **2007**, *104* (39), 15230.
(32) Travkova, O. G.; Moehwald, H.; Brezesinski, G. The interaction of antimicrobial peptides with membranes. *Adv. Colloid Interface Sci.* **2017**, *247*, 521−532.
(33) Liu, S. P.; Zhou, L.; Lakshminarayanan, R.; Beuerman, R. W. Multivalent Antimicrobial Peptides as Therapeutics: Design Principles and Structural Diversities. *Int. J. Pept Res. Ther* **2010**, *16* (3), 199−213.
(34) Chen, C.; Chen, Y.; Yang, C.; Zeng, P.; Xu, H.; Pan, F.; Lu, J. R. High Selective Performance of Designed Antibacterial and Anticancer Peptide Amphiphiles. *ACS Appl. Mater. Interfaces.* **2015**, *7* (31), 17346−17355.
(35) Alves, A. C.; Ribeiro, D.; Nunes, C.; Reis, S. Biophysics in cancer: The relevance of drug-membrane interaction studies. *BBA Libr.* **2016**, *1858* (9), 2231−2244.
(36) Zhou, C.; Wang, F.; Chen, H.; Li, M.; Qiao, F.; Liu, Z.; Hou, Y.; Wu, C.; Fan, Y.; Liu, L.; Wang, S.; Wang, Y. Selective Antimicrobial Activities and Action Mechanism of Micelles Self-Assembled by Cationic Oligomeric Surfactants. *ACS Appl. Mater. Interfaces.* **2016**, *8* (6), 4242−4249.
(37) Melo, M. N.; Ferre, R.; Castanho, M. A. R. B. Antimicrobial peptides: linking partition, activity and high membrane-bound concentrations. *Nat. Rev. Microbiol* **2009**, *7* (3), 245−250.
(38) Xing, H.; Loya-Perez, V.; Franzen, J.; Denton, P. W.; Conda-Sheridan, M.; Rodrigues de Almeida, N. Designing peptide amphiphiles as novel antibacterials and antibiotic adjuvants against gram-negative bacteria. *Bioorg. Med. Chem. Lett.* **2023**, *94*, No. 117481.
(39) Pereira, A. J.; Xing, H.; de Campos, L. J.; Seleem, M. A.; de Oliveira, K. M. P.; Obaro, S. K.; Conda-Sheridan, M. Structure-Activity Relationship Study to Develop Peptide Amphiphiles as Species-Specific Antimicrobials. *Chem. − Eur. J.* **2024**, *30* (15), No. e202303986.
(40) Dathe, M.; Nikolenko, H.; Meyer, J.; Beyermann, M.; Bienert, M. Optimization of the antimicrobial activity of magainin peptides by modification of charge. *FEBS Lett.* **2001**, *501* (2−3), 146−50.
(41) Loffredo, M. R.; Savini, F.; Bobone, S.; Casciaro, B.; Franzyk, H.; Mangoni, M. L.; Stella, L. Inoculum effect of antimicrobial peptides. *Proc. Natl. Acad. Sci. U.S.A.* **2021**, *118* (21), No. e2014364118.
(42) White, L. J.; Boles, J. E.; Allen, N.; Alesbrook, L. S.; Sutton, J. M.; Hind, C. K.; Hilton, K. L. F.; Blackholly, L. R.; Ellaby, R. J.; Williams, G. T.; Mulvihill, D. P.; Hiscock, J. R. Controllable hydrogen bonded self-association for the formation of multifunctional antimicrobial materials. *J. Mater. Chem. B* **2020**, *8* (21), 4694−4700.
(43) Pandurangan, K.; Kitchen, J. A.; Blasco, S.; Paradisi, F.; Gunnlaugsson, T. Supramolecular pyridyl urea gels as soft matter with antibacterial properties against MRSA and/or E. coli. *Chem. Commun.* **2014**, *50* (74), 10819−10822.
(44) Barman, S.; Konai, M. M.; Samaddar, S.; Haldar, J. Amino Acid Conjugated Polymers: Antibacterial Agents Effective against Drug-Resistant Acinetobacter baumannii with No Detectable Resistance. *ACS Appl. Mater. Interfaces.* **2019**, *11* (37), 33559−33572.
(45) te Winkel, J. D.; Gray, D. A.; Seistrup, K. H.; Hamoen, L. W.; Strahl, H. Analysis of Antimicrobial-Triggered Membrane Depolarization Using Voltage Sensitive Dyes. *Front. Cell Dev. Biol.* **2016**, *4*, 29.
(46) Rosenberg, M.; Azevedo, N. F.; Ivask, A. Propidium iodide staining underestimates viability of adherent bacterial cells. *Sci. Rep.* **2019**, *9* (1), 6483.
(47) Wieprecht, T.; Dathe, M.; Beyermann, M.; Krause, E.; Maloy, W. L.; MacDonald, D. L.; Bienert, M. Peptide Hydrophobicity Controls the Activity and Selectivity of Magainin 2 Amide in Interaction with Membranes. *Biochemistry* **1997**, *36* (20), 6124−6132.

https://doi.org/10.1021/acs.biomac.3c01463
Biomacromolecules 2024, 25, 2823−2837